Available online at www.sciencedirect.com
ScienceDirect
Journal of Sound and Vibration 309 (2008) 20–39
JOURNAL OF SOUND AND VIBRATION
www.elsevier.com/locate/jsvi

A finite element approach for the simulation of tire rolling noise

Maik Brinkmeier[a], Udo Nackenhorst[a], Steffen Petersen[b], Otto von Estorff[b,*]

[a]*Institute of Mechanics and Computational Mechanics, University of Hannover, Appelstraße 9A, D-30167 Hannover, Germany*
[b]*Modelling and Computation, Hamburg University of Technology, Denickestraße 17, D-21073 Hamburg, Germany*

Received 28 July 2005; received in revised form 6 April 2006; accepted 20 November 2006

Abstract

A physically motivated modeling process for the prediction of noise radiated from rolling tires is presented. The overall simulation procedure is based on a decomposition into the nonlinear stationary rolling case, the eigenvalue analysis in the deformed state, and the calculation of the noise radiation including a modal superposition approach with an excitation by deterministic functions. The simulations cover detailed finite element models of the tire/road system. This allows for various parameter studies with respect to noise reduction potentials. The new model is applied to representative numerical examples, and its accuracy as well as its efficiency are discussed.

1. Introduction

Regarding the reduction of traffic noise, significant progress has been achieved with respect to the sound radiation of the powertrain of vehicles. As a consequence, the rolling noise of tires has become the main source at speeds above 40 km/h for passenger cars and 60 km/h for trucks. Hence, no significant reduction of the noise radiated from vehicles seems possible without decreasing the tire/road noise.

In order to support the efficient design of low noise tires as well as roads, the development of simulation tools, employing virtual prototypes of the tire/road system, is essential. However, currently no physically based and validated model exists that may be used to determine the sound radiation from rolling vehicle tires with reasonable accuracy in the relevant frequency range. This is primarily due to the complexity of the tire structure and the various effects contributing to the overall noise. A comprehensive study including measurements, statistics and simulations of both tires and roads as well as tire/road systems can be found in Ref. [1]. Models including empirical and structural approaches are presented in the works [2–4], where the tire is represented by plate or shell structures. These simplifications include the benefit of a rather small computational effort but obviously limit the predictions regarding the influence of sophisticated constructional components of modern tires.

A state-of-the-art simulation tool for static and stationary rolling analysis of rolling tires is the finite element method. In this contribution, a special Arbitrary Lagrangian Eulerian (ALE) approach is used to describe

*Corresponding author. Tel.: +49 40 42878 3032; fax: +49 40 42878 4353.
E-mail address: estorff@tu-harburg.de (O. von Estorff).
URL: http://www.mub.tu-harburg.de (O. von Estorff).

0022-460X/$ - see front matter
doi:10.1016/j.jsv.2006.11.040

rolling bodies in a relative kinematic sense as presented in Ref. [5]. Hence, any grade of detail is possible for the discretization of the structure, limited only by the computational equipment. For example, the influence of cord angles in composite layers of the tire, of the inflation, or of the rotational speed on the deflection can be examined with arbitrary accuracy.

The dynamic behavior of tires is modeled within a modal superposition approach assuming small vibrational amplitudes. Methods for the solution of the underlying complex valued eigenproblems can be found in Refs. [6,7]. The cost of the eigenvalue analysis is determined by the matrices provided by the finite element method. Additional effort arises from the necessity of using complex numbers and solving large-scale systems of linear equations. For the excitation of the system, measurements of real road textures are analyzed resulting in multi-frequency harmonic functions. These are the cause for the operational vibration of the tire on a specific road.

The computations for the acoustic part of the overall model are based on a combined finite/infinite element approach. An optimized variant [8] of the so-called mapped wave envelope elements [9], also known as Astley–Leis elements, is employed. The optimized infinite elements allow for a stable and extremely efficient solution process. This is essential in the case of a simulation of the overall tire/road noise for certain states of rolling, where computations for numerous frequency steps have to be carried out. An assessment of the efficiency and robustness of the infinite elements employed in this contribution is given in Ref. [10]. Meanwhile, these improved infinite elements are generally available as part of the high-performance FE-library libMesh [11].

The current paper is organized as follows: first, the overall model and the underlying computational strategy is outlined. Subsequently, terse descriptions of the employed numerical methods for the structural and the acoustic analyses are given. Since the computational costs of the underlying methods are somewhat crucial for the overall simulation procedure, some emphasis is given to the efficiency of the numerical approaches. Then, the applicability of the numerical model for simulating the tire/road noise is demonstrated and discussed based on representative numerical examples. Final remarks are given in the conclusions.

2. Preliminary remarks on the finite element model for tire/road noise

Despite the fast increase of computer performance over the last decades, it is still not possible to simulate the complete nonlinear dynamic behavior of rolling tires and the subsequent sound radiation directly. A significant reduction of the computational cost can be achieved by employing a modal superposition technique. This leads to a computational strategy, where the tire/road noise is analyzed in several subsequent steps. First, in a nonlinear steady-state rolling analysis the deformation of the tire in contact with a plane road is computed using finite elements within an ALE formulation, including effects of inertia due to rotation and pressure loads due to the inflation. The next step is a complex eigenvalue analysis of the gyroscopic system. The homogeneous equation of motion is transformed into a quadratic eigenvalue problem, which yields complex eigenvectors interpreted as traveling waves rather than standing vibrations, while the rotational speed influences the eigenvalues. Then a modal superposition is performed, resulting in the dynamic response of the system caused by the excitation. The tire is excited by the roughness of the road surface. This is taken into account in the contact region using a deterministic description by means of a discrete Fourier analysis of texture measurements, yielding a frequency spectrum with amplitudes and corresponding phase displacements. The meaningful parts of the spectrum are extracted and used for the excitation function.

After the determination of the tire dynamics, the sound radiation is computed in the acoustic part of the model. In this step, the vibrations on the tire surface are extracted and the normal velocity data are taken as boundary conditions for the acoustic simulations. Note that the structural dynamics is described a priori in spatially fixed coordinates. This enables a rather straightforward transfer of the vibration data onto the acoustic fluid domain. In addition, the acoustic properties of the road surface may also be considered by means of admittance or impedance boundary conditions.

Summarizing, the following steps are performed in order to simulate the noise generated and radiated by rolling tires:

- computation of the nonlinear stationary rolling process,
- eigenvalue analysis for the steady state of the rolling tire,

- determination of the excitation due to the texture of the road surface,
- computation of the operational vibrations with modal superposition, and
- noise radiation analysis.

The present work describes a first step in the physically based finite element analysis of the high-frequency dynamics of rolling tires. A slick tire is modeled, because tread tires may only be modeled approximately within the ALE framework that is used here. However, these investigations already enable studies on the interaction of the tire and the road with respect to principle constructive parameters. At the current stage, the understanding of basic mechanisms is emphasized. Further refinement of the model, e.g. considering tractive rolling with partial slip or frequency dependent material parameters, is intended for the near future.

3. Governing relations

3.1. Stationary rolling

A special ALE formulation is used for the stationary description of rolling. In Fig. 1 the decomposition of motion used in the ALE description is depicted. The mapping between the configurations splits into pure rigid body motion χ and deformation $\hat{\phi}$, here applied to the gradient of deformation for example,

$$\mathbf{F} = \frac{\partial \mathbf{x}}{\partial \mathbf{X}} = \frac{\partial \mathbf{x}}{\partial \boldsymbol{\chi}} \cdot \frac{\partial \boldsymbol{\chi}}{\partial \mathbf{X}} = \hat{\mathbf{F}} \cdot \tilde{\mathbf{R}}, \tag{1}$$

with the benefit of having a deformable but fixed finite element mesh, while the material is rotating inside. The material time derivative is split additively into relative and convective part,

$$\frac{\mathrm{d}()}{\mathrm{d}t} = \frac{\partial()}{\partial t} + \mathrm{Grad} \cdot \mathbf{w}, \tag{2}$$

with the guiding velocity $\mathbf{w}$. Since the relative part $\partial()/\partial t$ disappears for stationary processes, these can be described in a time independent manner.

The equation of motion of the continuum in conjunction with laws for deformation and constitutive description of material behavior as well as boundary conditions for traction and displacement provides a boundary value problem. This is iteratively solved in a weak formulation with consistent linearization and discretization by finite elements. A detailed description of the theory can be found in Ref. [5]. Finally,

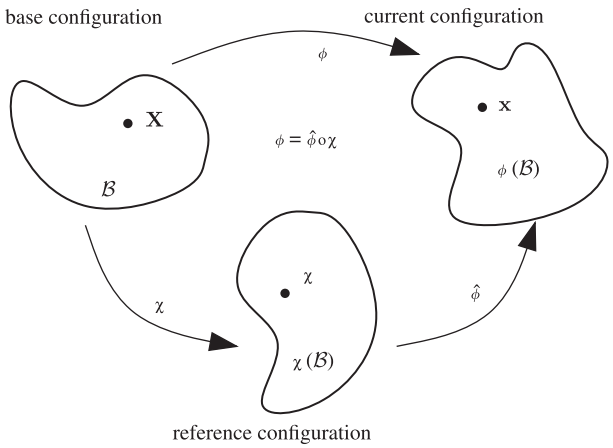

Fig. 1. Introducing rotated reference configuration.

the equation

$$({}^{t}\mathbf{K}-\mathbf{W})\Delta\hat{\boldsymbol{\varphi}}={}^{t+\Delta t}\hat{\mathbf{f}}_{\mathrm{e}}+{}^{t}\hat{\mathbf{f}}_{\mathrm{i}}-{}^{t}\hat{\mathbf{f}}_{\sigma}, \tag{3}$$

with the stiffness matrix ${}^{t}\mathbf{K}$, the ALE-inertia matrix $\mathbf{W}$ and forces of external loads ${}^{t+\Delta t}\hat{\mathbf{f}}_{\mathrm{e}}$, ALE-inertia ${}^{t}\hat{\mathbf{f}}_{\mathrm{i}}$ and internal stresses ${}^{t}\hat{\mathbf{f}}_{\sigma}$ has to be solved for the incremental displacement $\Delta\hat{\boldsymbol{\varphi}}$ by a Newton–Raphson scheme for the stationary rolling step including a contact formulation for the structure with a road.

3.2. Eigenvalue analysis

The eigendynamics is described by the homogenous finite element equation of motion

$$\mathbf{M}\ddot{\boldsymbol{\phi}}+\mathbf{G}\dot{\boldsymbol{\phi}}+\tilde{\mathbf{K}}\boldsymbol{\phi}=0,\quad \tilde{\mathbf{K}}={}^{t}\mathbf{K}-\mathbf{W},\quad \mathbf{G}=-\mathbf{G}^{\mathrm{T}}, \tag{4}$$

with the mass matrix $\mathbf{M}$, gyroscopic matrix $\mathbf{G}$ and vibrations $\boldsymbol{\phi}$ measured relative to the deformation state of stationary rolling. The harmonic ansatz

$$\boldsymbol{\phi}=\mathbf{z}\,\mathrm{e}^{\lambda t},\quad \lambda=\mathrm{i}\omega \tag{5}$$

yields a quadratic eigenvalue problem of the form

$$\mathbf{Q}(\lambda)\mathbf{z}:=(\lambda^{2}\mathbf{M}+\lambda\mathbf{G}+\tilde{\mathbf{K}})\mathbf{z}=\mathbf{0}. \tag{6}$$

Since the gyroscopic matrix is skew-symmetric, it is convenient to use the following linearization in the state space

$$\left(\begin{bmatrix}\mathrm{i}\mathbf{G} & \tilde{\mathbf{K}}\\ \tilde{\mathbf{K}} & \mathbf{0}\end{bmatrix}-\omega\begin{bmatrix}\mathbf{M} & \mathbf{0}\\ \mathbf{0} & \tilde{\mathbf{K}}\end{bmatrix}\right)\bar{\mathbf{z}}=\mathbf{0},\quad \bar{\mathbf{z}}=\begin{bmatrix}\omega\mathbf{z}\\ \mathbf{z}\end{bmatrix}, \tag{7}$$

to maintain the hermitian properties of the quadratic eigenvalue problem in the generalized linear eigenvalue problem. This is solved with the implicitly restarted Arnoldi method available with the large-scale eigenvalue solver package ARPACK [6]. Keeping the hermitian symmetry reduces the storage requirements for the matrices and their preconditioners and produces equivalence of left and right eigenvectors, which is also a benefit in the sense of data handling as well as less computational cost.

For the solution of the eigenproblem the so called shift-invert mode is used. Most solution methods for eigenproblems converge to the extremal eigenvalues. If the eigenproblem is inverted, the smallest eigenvalues in the vicinity of zero are computed. The shift-invert mode enhances this in the way that the eigenvalues near a given shift are calculated. Thus, this is an effective method in order to compute the eigenvalues and eigenvectors in the frequency range that is of importance for tire/road systems.

During the iterative process of the implicitly restarted Arnoldi method with the given shift value σ the linear system of equations

$$\begin{bmatrix}\mathrm{i}\mathbf{G}-\sigma\mathbf{M} & \tilde{\mathbf{K}}\\ \tilde{\mathbf{K}} & -\sigma\tilde{\mathbf{K}}\end{bmatrix}\begin{bmatrix}\mathbf{x}_1\\ \mathbf{x}_2\end{bmatrix}=\begin{bmatrix}\mathbf{b}_1\\ \mathbf{b}_2\end{bmatrix} \tag{8}$$

has to be solved for the vector $\mathbf{x}$ multiple times. Regarding the memory requirements, the solution of Eq. (8) with twice the dimension of the original system in Eq. (7) seems inefficient, especially because the complex numbers need twice the storage of real numbers. Therefore, the system is transformed back to the quadratic form, resulting in the following two operations with less computational cost:

$$\mathbf{x}_2=\mathbf{Q}^{-1}[\mathbf{M}\mathbf{b}_1-(\mathrm{i}\mathbf{G}-\sigma\mathbf{M})\mathbf{K}^{-1}\mathbf{b}_2], \tag{9}$$

$$\mathbf{x}_1=\mathbf{K}^{-1}\mathbf{b}_2+\sigma\mathbf{x}_2. \tag{10}$$

Next, an incomplete Cholesky factorization is used as preconditioner for the matrices $\mathbf{Q}$ and $\mathbf{K}$ in conjunction with a iterative method like BiCGSTAB. This is an effective way for the solution of the linear system of equations, since the preconditioner for the stiffness matrix $\mathbf{K}$ is always the same, while the preconditioner for the quadratic form $\mathbf{Q}$ only has to be recalculated when a new shift σ is applied. Regarding the overall

computational cost, the solution of the linear system of Eqs. (9) and (10) takes the largest portion of the total computation time, varying from 50% to 95% depending on the problem size and the size of the subspace chosen for the eigenvalue analysis. Also, most of the memory is required for preconditioners due to the fill-in of sparse matrix entries during incomplete Cholesky factorization. Empirical studies have shown that for practical purposes a preconditioner with good convergence has a fill-in factor of 5–20, resulting in memory requirements of some gigabytes for common tire models.

3.3. Excitation caused by road texture

Filtering and discrete Fourier transformation is applied to digitized data of road surfaces resulting in harmonic excitation functions,

$$\mathbf{u}(t) = \sum_j \hat{\mathbf{u}}_j \mathrm{e}^{\mathrm{i}(\varphi_j + \omega_j^{\mathrm{ex}} t)}. \tag{11}$$

These displacements are applied to the contact nodes of the previously calculated modal model for each separate amplitude vector $\hat{\mathbf{u}}_j$ and excitation frequency ω_j^{ex}. The phase angle φ_j of the contact nodes is determined by the rotational speed of the tire in circumferential direction and randomly shifted in lateral directions in the footprint. With the stiffness related to the contact patch $\mathbf{K}_{\mathrm{c}}$, a corresponding force vector $\mathbf{f}(t)$ is applied to the right-hand side of the equation of motion,

$$\mathbf{M}\ddot{\boldsymbol{\phi}} + \mathbf{G}\dot{\boldsymbol{\phi}} + \tilde{\mathbf{K}}\boldsymbol{\phi} = \mathbf{f}(t), \quad \mathbf{f}(t) = -\mathbf{K}_{\mathrm{c}}\mathbf{u}(t). \tag{12}$$

Again, the usage of the equivalent linearized form

$$\begin{bmatrix} \mathrm{i}\mathbf{G} & \tilde{\mathbf{K}} \\ \tilde{\mathbf{K}} & \mathbf{0} \end{bmatrix} \bar{\boldsymbol{\phi}} - \begin{bmatrix} \mathbf{M} & \mathbf{0} \\ \mathbf{0} & \tilde{\mathbf{K}} \end{bmatrix} \dot{\bar{\boldsymbol{\phi}}} = \begin{bmatrix} \mathbf{f}(t) \\ \mathbf{0} \end{bmatrix}, \quad \bar{\boldsymbol{\phi}} = \begin{bmatrix} \dot{\boldsymbol{\phi}} \\ \boldsymbol{\phi} \end{bmatrix}, \tag{13}$$

decouples the system with the modal matrix $\bar{\mathbf{Z}}$, the diagonal matrix of eigenvalues $\boldsymbol{\Omega}$ and the generalized coordinates $\bar{\mathbf{q}}$,

$$\bar{\boldsymbol{\phi}} = \sum_j \bar{\mathbf{Z}}\bar{\mathbf{q}}_j, \quad \bar{\mathbf{Z}} = \begin{bmatrix} \mathbf{Z}\boldsymbol{\Omega} \\ \mathbf{Z} \end{bmatrix}, \quad \boldsymbol{\Omega} = \mathrm{diag}(\omega_i) \tag{14}$$

yielding first-order differential equations

$$\omega_i \bar{q}_{ij} - \dot{\bar{q}}_{ij} = \bar{f}_{ij}. \tag{15}$$

Furthermore, a harmonic ansatz is taken for the generalized coordinates to get the stationary solution. With the properties of orthogonality of the linear eigenproblem (7) one obtains

$$\bar{\mathbf{q}}_j = (\mathrm{i}\boldsymbol{\Omega} - \mathrm{i}\omega_j^{\mathrm{ex}}\mathbf{I})^{-1} \bar{\mathbf{Z}}^H \hat{\mathbf{f}} \mathrm{e}^{\mathrm{i}(\varphi_j + \omega_j^{\mathrm{ex}} t)} \tag{16}$$

and for the operational vibration of the tire with modal superposition

$$\boldsymbol{\phi}(t) = \sum_j \mathbf{Z}(\mathrm{i}\boldsymbol{\Omega} - \mathrm{i}\omega_j^{\mathrm{ex}}\mathbf{I})^{-1} \boldsymbol{\Omega}\mathbf{Z}^H \hat{\mathbf{f}} \mathrm{e}^{\mathrm{i}(\varphi_j + \omega_j^{\mathrm{ex}} t)}. \tag{17}$$

To overcome the resonance case, a reasonable small value δ can be used as virtual damping, avoiding numerical problems when inverting the diagonal matrix

$$(\mathrm{i}\boldsymbol{\Omega} - \mathrm{i}\omega_j^{\mathrm{ex}}\mathbf{I})^{-1} \to (-\delta\mathbf{I} + \mathrm{i}\boldsymbol{\Omega} - \mathrm{i}\omega_j^{\mathrm{ex}}\mathbf{I})^{-1}. \tag{18}$$

This damping is mathematically founded because negative real parts appear in the eigenvalues of damped structural systems, when the eigenproblem is stable.

Finally, the structural data, namely geometry, displacements and eigenvectors of the tire surface as well as the generalized coordinates are used for the sound radiation analysis.

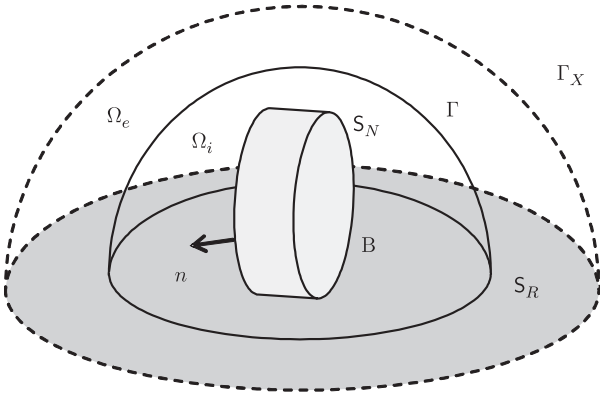

Fig. 2. Geometry of the exterior acoustic problem.

3.4. Exterior boundary value problem for the Helmholtz equation

The starting point for the noise radiation analysis is the exterior boundary value problem illustrated in Fig. 2. Consider a three-dimensional vibrating body B in a half-space bounded by the plane S_R. The surface of B is denoted by S_N. The exterior domain Ω is decomposed into an interior and exterior part through the envelope Γ. The time-harmonic pressure p in Ω_i and Ω_e is governed by the Helmholtz equation

$$\Delta p + k^2 p = 0, \tag{19}$$

where $k = \omega/c$ is the wavenumber, and ω is the angular frequency. The normal vector n of the surface $\mathsf{S} = \mathsf{S}_N \cup \mathsf{S}_R$ points into the domain Ω. Corresponding time-harmonic boundary conditions are prescribed on S, namely Neumann and Robin boundary conditions, respectively,

$$v_n = v_n^o \quad \text{on } \mathsf{S}_N, \tag{20}$$

$$\frac{v_n}{p} = \alpha \frac{1}{\rho c} \quad \text{on } \mathsf{S}_R, \tag{21}$$

where v_n is the normal velocity, c is the wave speed, ρ is the fluid density and α is an absorption coefficient normal to the surface. To enforce uniqueness of solutions for Eq. (19) on Ω with boundary conditions given in Eqs. (20) and (21), a radiation condition is enforced on the artificial boundary Γ_X, which is supposed to limit the exterior domain Ω_e

$$\mathrm{i}kp + \frac{\partial p}{\partial r} = o(X^{-(d-1)/2}) \quad \text{on } \Gamma_X, \tag{22}$$

where $d = 3$ is the spatial dimension of the problem. In the limit $X \to \infty$ the domain Ω_e renders unbounded, and Eq. (22) will lead to the Sommerfeld condition.

Note, that the most general statement would also consider Dirichlet boundary conditions $p = p^o$. However, since these conditions rarely occur for practical problems of acoustic radiation and scattering, they are not considered here.

3.5. Weak formulation of the Helmholtz problem

The weak formulation of the boundary value problem given by Eqs. (19)–(22) may be derived using a weighted residual technique or by means of variational formulations. Introducing test functions $\bar{q}$ and trial

functions p, and employing Green's theorem, the variational form of Eqs. (19)–(22) reads

$$\int_{\Omega}(\nabla p\cdot\nabla\bar{q}-k^2p\bar{q})\,\mathrm{d}V-\int_{\mathsf{S}_N}\mathrm{i}\rho\omega v_n^o p\bar{q}\,\mathrm{d}\mathsf{S}$$
$$-\int_{\mathsf{S}_R}\mathrm{i}k\alpha p\bar{q}\,\mathrm{d}\mathsf{S}+\int_{\Gamma_X}(\mathrm{i}kp\bar{q}-o(X^{-(d-1)/2}))\,\mathrm{d}\mathsf{S}=0. \tag{23}$$

The infinite element formulation employed here is based on the Astley–Leis framework, where the test trial functions, taken from weighted Sobolev spaces, satisfy the radiation condition in Eq. (22). Thus, the last integral in Eq. (23) may be dropped and the weak form of Eqs. (19)–(22) is finally given by

$$\int_{\Omega}(\nabla p\cdot\nabla\bar{q}-k^2p\bar{q})\,\mathrm{d}V-\int_{\mathsf{S}_N}\mathrm{i}\rho\omega v_n^o p\bar{q}\,\mathrm{d}\mathsf{S}-\int_{\mathsf{S}_R}\mathrm{i}k\alpha p\bar{q}\,\mathrm{d}\mathsf{S}. \tag{24}$$

It now remains to insert appropriate test and trial functions.

3.6. Infinite element formulation

While the FEM is well suited for the analysis of structures, the simulation of unbounded domains is more difficult to achieve. This means that in vibro-acoustics special care is necessary to simulate the response of an unbounded acoustic fluid coupled to a vibrating structure. Various tools are available for this, among which the best known are the boundary element method (BEM) with special non-reflecting boundary conditions and infinite elements. Already developed in the late 1970s, the latter has gained remarkable popularity in recent years and today several formulations exist. Reviews of the most commonly used formulations may be found in Refs. [12,13], whereas a rather recent concept is given in Ref. [14]. Investigations of the Astley–Leis elements, emphasizing radiation and scattering problems in an acoustic half-space, may be found in Ref. [15].

Compared to the BEM, a major advantage of the combined finite/infinite element approach is that the infinite elements preserve the banded structure of the system matrices, enabling for extremely efficient solution procedures. As a consequence, the infinite element approach may surpass standard BEM formulations in terms of computational efficiency [16]. Additionally, the infinite elements formulation employed here may be easily transformed to the time domain and with some slight modifications this method provides stable simulations of transient exterior acoustics [17], whereas transient BEM formulations are known to behave rather unstable.

The interior part Ω_i is discretized with conventional elements, including the common polynomial shape functions N_i for the test and trial functions $\bar{q}$ and p, respectively, i.e.

$$p\approx\sum_{i=1}^{n}p_iN_i, \tag{25}$$

where n is the number of generalized unknowns p_i associated with the current finite element. The infinite elements employed in this contribution build up on the so-called Astley–Leis elements, however with modifications regarding the polynomial approximation functions in radial direction. These elements are based on a Petrov–Galerkin scheme, i.e., complex conjugates of the trial functions are used as test functions. Similarly to [9], the trial functions may be written in the form

$$p\approx\sum_{i=1}^{n}p_i\Phi_i\mathrm{e}^{-\mathrm{i}k\mu}, \tag{26}$$

where n is the number of generalized unknowns p_i associated with the current infinite element and μ is a phase-like term. The function Φ_i is defined by

$$\Phi_i=\frac{1}{r}S_jP_k \tag{27}$$

consisting of the base approximation S_i, independent of the radial direction r, the radial approximation P_k, and an additional factor assuring that the radiation condition is satisfied. The subscripts j,k in Eq. (27) may be

chosen such that the combination of the base and the radial approximation functions yields the correct polynomial Φ_i. The test functions may be written as

$$\bar{q} \approx \frac{1}{r^2} \sum_{i=1}^{n} p_i \Phi_i \mathrm{e}^{+\mathrm{i}k\mu}. \tag{28}$$

Using the complex conjugate of the oscillatory term in Eq. (26), these terms cancel out and conventional numerical quadrature rules may be employed when integrating over an infinite element. The additional weight $D = (1/r)^2$ in Eq. (28) assures that the variational problem in Eq. (24) is well-defined [18].

The discrete version of Eq. (24) may then be written as

$$\mathbf{A}(\omega)\mathbf{p} := [\mathbf{K}_A + (i\omega)\mathbf{C}_A - \omega^2 \mathbf{M}_A]\mathbf{p} = \mathbf{f}_A, \tag{29}$$

where $\mathbf{K}_A$, $\mathbf{C}_A$, and $\mathbf{M}_A$ are frequency independent acoustic system matrices and only have to be assembled once during the simulation. These matrices are also referred to as inverse mass, admittance and compressibility operator, respectively (note, in some literature the system matrices are denoted as acoustic stiffness, damping and mass matrix, due to their counterparts in structural analysis). The vector $\mathbf{p}$ contains the unknown pressure values, and $\mathbf{f}_A$ is the load vector, representing the tire dynamics on the surface. For each excitation frequency, the right-hand side vector is computed using the eigenvectors on the tire surface weighted with the corresponding generalized coordinates (cf. Section 3.3) and the overall matrix is computed by summing up the acoustic system matrices. In the interior part Ω_i the contributions to the system matrices are given by

$$K_{ij} = \int_{\Omega^e} \nabla N_i \nabla N_j \, \mathrm{d}V, \tag{30}$$

$$M_{ij} = 1/c^2 \int_{\Omega^e} N_i N_j \, \mathrm{d}V, \tag{31}$$

$$C_{ij} = \rho \int_{\mathsf{S}_R^e} \alpha N_i N_j \, \mathrm{d}S. \tag{32}$$

The right-hand side vector is computed from the normal velocities on the tire surface by

$$f_i = -\mathrm{i}\omega \int_{\mathsf{S}_N^e} \rho v_n^o N_i \, \mathrm{d}S. \tag{33}$$

Contributions from an infinite element in the exterior Ω_e are given by

$$K_{ij} = \int_{\Omega^e} (\nabla D \Phi_i + \nabla \Phi_i D) \nabla \Phi_j \, \mathrm{d}V, \tag{34}$$

$$M_{ij} = 1/c^2 \int_{\Omega^e} (1 - (\nabla \mu \nabla \mu)) \Phi_i \Phi_j D \, \mathrm{d}V, \tag{35}$$

$$C_{ij} = 1/c \int_{\Omega^e} (\nabla \mu \nabla \Phi_j) D \Phi_i - (\nabla D \nabla \mu) \Phi_i \Phi_j - (\nabla \Phi_i \nabla \mu) D \Phi_j \, \mathrm{d}V, \tag{36}$$

$$+ 1/c \int_{\mathsf{S}_R^e} \alpha \Phi_i \Phi_j D \, \mathrm{d}S. \tag{37}$$

Including a mapping with $a/r = (1 - v)/2$, where a is the distance from the infinite element origin to the base of the infinite element and $2a$ corresponds to the origin of v [19], it appears that terms arising in the integral expressions of Eqs. (34)–(36) perfectly match the orthogonality property of the Jacobi polynomial $P^{\alpha,\beta}$ with $\alpha = 2$ and $\beta = 0$

$$\int_{-1}^{1} (1 - v)^2 P_i^{2,0} P_j^{2,0} \, \mathrm{d}v = \mu_i \delta_{ij}, \tag{38}$$

where μ_i is a given constant and δ_{ij} is the Kronecker delta. Compared to infinite elements based on Legendre Polynomials, this element type provides lower conditioning of the overall system matrix and leads to more

efficient simulations, in combination with Krylov solvers, such as, e.g., the generalized minimal residual method (GMRES), details are given in Ref. [16]. It should be noted that the method employed here assumes the tire to be fixed in space, which yields a situation similar to a tire rolling on a drum. Infinite element formulations including moving media may be found in Refs. [20,21].

4. Numerical examples

Since the stationary rolling analysis of tires is state-of-the-art, the following examples focus on the eigendynamics of gyroscopic systems, simulation of transfer functions, description and analysis of surface textures, operation of the tire on the road and sound radiation.

4.1. Eigendynamics of truck tire

To demonstrate the ability of the eigenvalue solver to handle large-scale problems, a truck tire with 140 700 degrees of freedom, 41 800 elements and 18 different material groups has been analyzed. The tire is rolling on a plane road with 50 km/h and is inflated with 0.9 MPa. For the eigenvalue analysis it is possible to compute some eigenvalues near a given shift. Fig. 3 provides an overview of typical eigenforms at frequencies near 0, 360 and 720 Hz. The deformation represents the real part of the eigenform and red color marks the maximum nodal amplitude. Remember, these complex eigenforms are not only vibrations but rather circumferentially moving waves. The eigenforms with the lowest eigenfrequency are the well known bending modes of the belt, while in the mid-range the lateral modes become more and more dominant. At high frequencies the relatively soft parts of the tire, like the tread or the outer sidewall, have the highest amplitude.

4.2. Virtue of rotation

The simulations of the next sections were performed using a rather coarse model of a tire. The model consists of three material groups for sidewall, belt and tread, respectively, with a total of 3800 brick elements and 18 000 degrees of freedom. The computation includes inflation with 0.2 MPa and displacement driven contact with the road and has been carried out for the standing tire as well as for rotations corresponding to 40, 80 and 120 km/h.

Analytical investigations of a circular ring and measurements of a rotating glass [22] have shown that an eigenpair of a standing object is split into two eigenpairs due to the gyroscopic effect. In this sense, the rotational symmetric eigenforms like breathing modes are an exception. The eigenfrequency is increased or decreased by the product of the number of waveform and the rotational frequency, while the two eigenforms appear as counterrotating waves. In Fig. 4 an example for this effect can be observed. The two eigenforms with

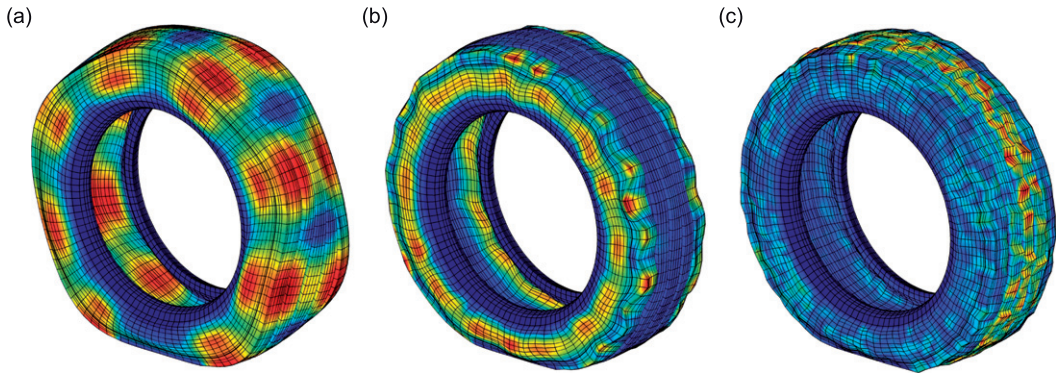

Fig. 3. Typical eigenforms of a truck tire.

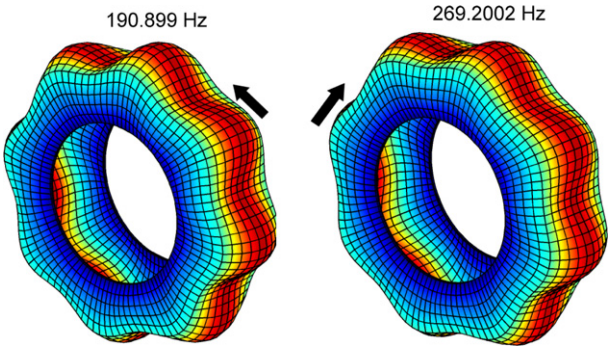

Fig. 4. Gyroscopic split of counterrotating eigenforms.

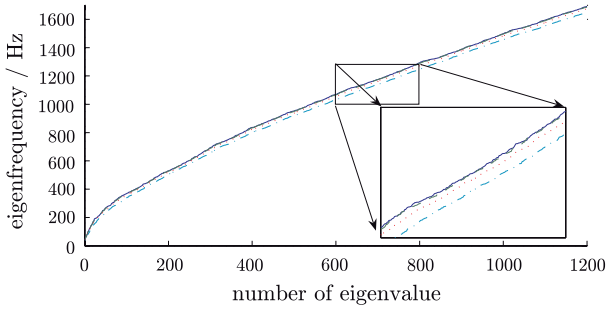

Fig. 5. Influence of the speed on the eigenvalues of the tire (— 0 km/h, - - 40 km/h, ··· 80 km/h, -·- 120 km/h).

circumferential harmonic wavenumber $n = 8$ are results of a tire without contact but rotating with $\omega = 31.7\,\mathrm{rad/s}$. The eigenfrequency of the related standing vibration would be $f_r = 230\,\mathrm{Hz}$ and the shift of the counterrotating eigenforms can be approximated by

$$\Delta f = \pm\frac{n\omega}{2\pi} = \pm 40.4\,\mathrm{Hz},$$

corresponding to the eigenfrequencies in Fig. 4. When the tire is in contact with the road, the affinity to a circular ring is broken and as a consequence the straight split into two eigenforms hardly occurs. Fig. 5 shows the 1200 lowest eigenfrequencies of a tire model, rolling on a road at different speeds. The main effect in this case is that increasing speed decreases the common eigenvalue distribution in the spectrum. Occasionally a gyroscopic split can be detected, when the contact state does not disturb the eigenmode.

4.3. Transfer functions

In this section examples of the frequency response of different nodes at the sidewall and the belt of the tire are presented, where a single node near the center of the upper belt is excited with unit forces in all three spatial directions, while the nodes of the contact patch are kept fixed. This simulates the setup of a point-shaker experiment. The comparison of calculated transfer functions with measurements, which were conducted by a laser Doppler vibrometer at given nodes with known excitation, may be used for validation of the model. The locations of the nodes are depicted in Fig. 6. The transfer functions presented in Figs. 7–10 are given in separate graphs for the vibrational magnitude in vertical (x) direction, driving (y) direction and axial (z) direction.

Fig. 7 shows the response of the node at the upper belt where the forces are induced into the tire. One may clearly identify the corresponding eigenmodes at the peaks of resonance and determine in which directions they interact with the excitation. With respect to the response of a node in the front of the belt depicted in

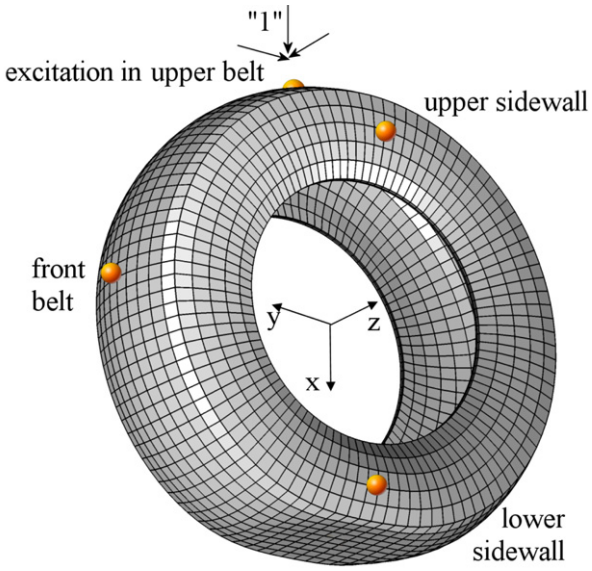

Fig. 6. Location of nodes for evaluation of the transfer functions.

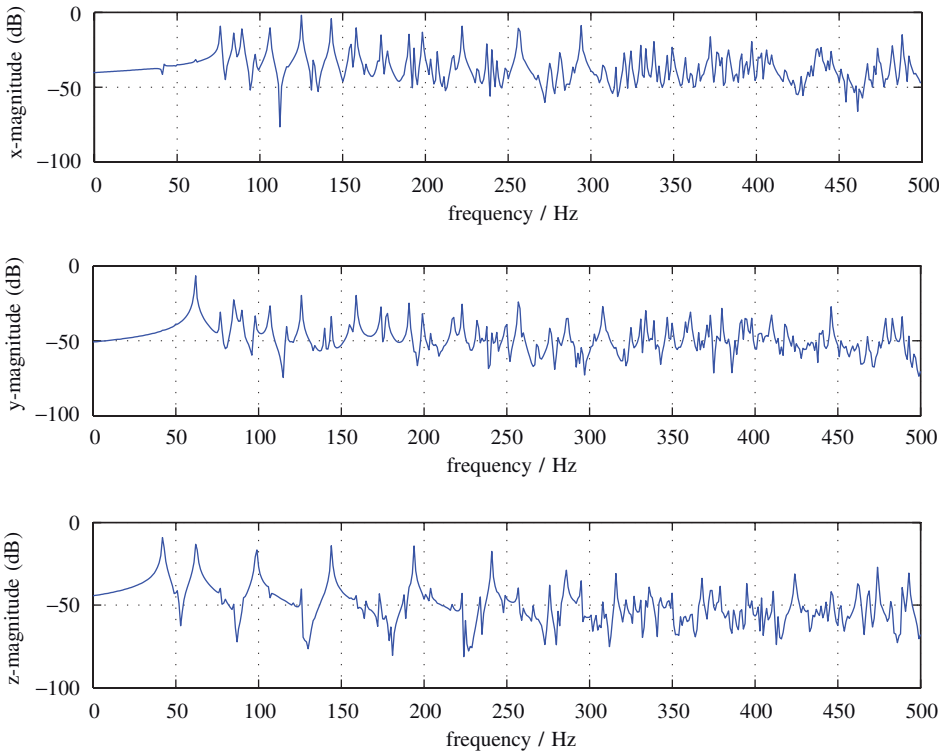

Fig. 7. Transfer functions of a node in the upper belt.

Fig. 8, it appears that the highest response of the belt modes can be observed in the frequency range up to 300 Hz. Above that frequency the amplitude drops. In contrast to this, the node in the upper sidewall in Fig. 9 has similar amplitudes at most eigenfrequencies, while the amplitude of the node in the lower sidewall, shown in Fig. 10, increases with the frequency.

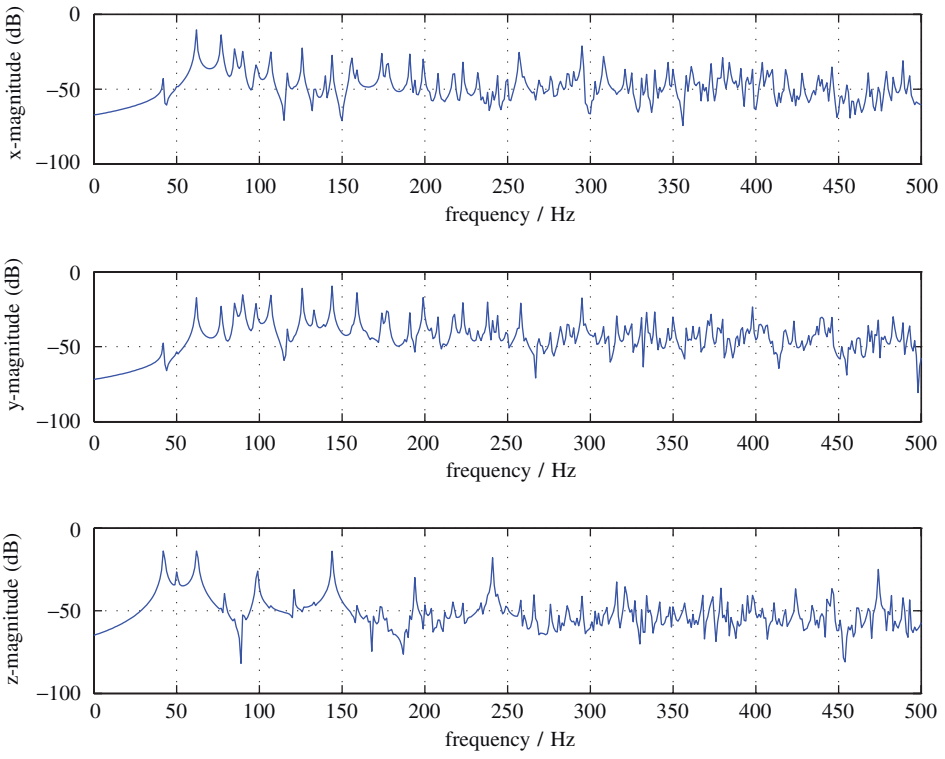

Fig. 8. Transfer functions of a node in the front belt.

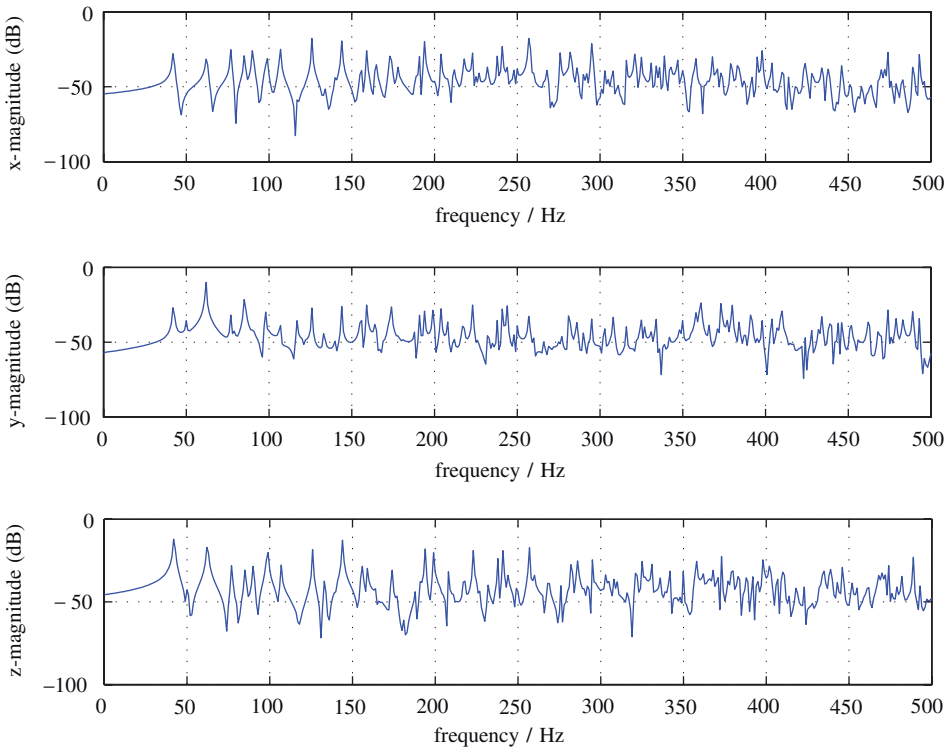

Fig. 9. Transfer functions of a node in the upper sidewall.

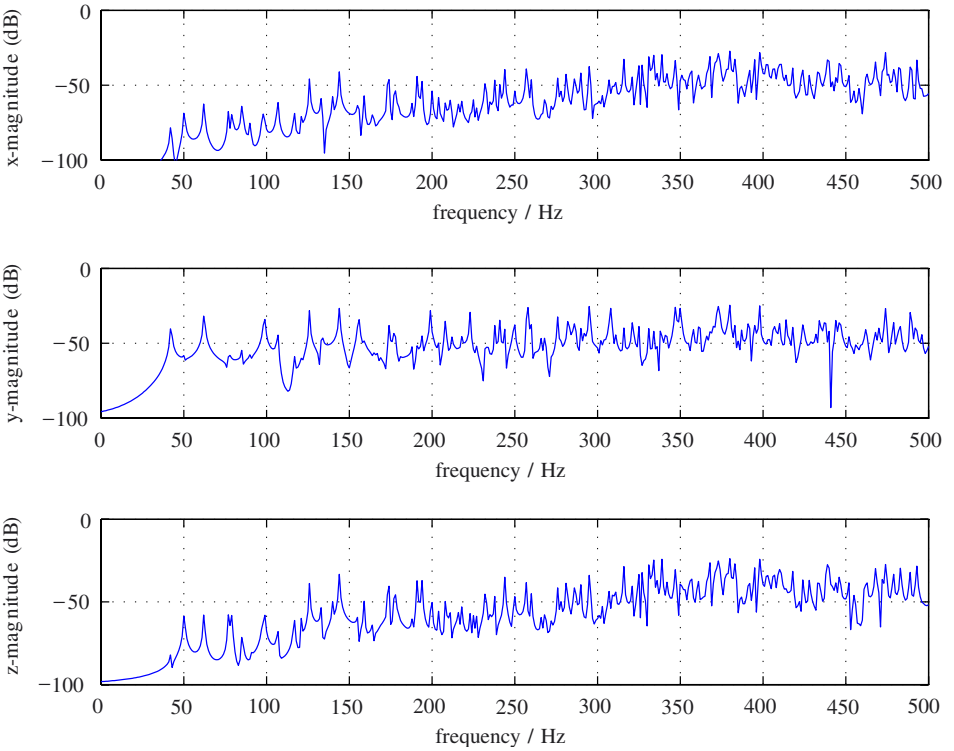

Fig. 10. Transfer functions of a node in the lower sidewall.

4.4. Characterization of surface textures

To get an appropriate frequency resolution in the discrete Fourier transformation, the window size of the measurements has to be rather large. The longest distance of surface textures measurements, available at the Bundesanstalt für Straßenwesen, yield the following spatial data:

$$n_p = 65\,536,$$

$$\Delta x = 0.5\,\text{mm},$$

$$\lambda^s_{\max} = (n_p - 1)\Delta x = 32\,767.50\,\text{mm},$$

$$f^s_{\min} = {\lambda^s_{\max}}^{-1} = 3.052 \times 10^{-5}\,\text{mm}^{-1},$$

where n_p is the number of samples, Δx is the sample length, $\lambda^{\text{s}}_{\max}$ the maximum wavelength, and $f^{\text{s}}_{\min}$ the minimum spatial frequency (the resolution). The highest measurable frequency, according to Nyquist, is half the sampling frequency

$$f^{\text{s}}_{\max} = \frac{f^{\text{s}}_{\text{s}}}{2} = \frac{1}{2\Delta x} = 1\,\text{mm}^{-1}.$$

Connecting the frequency in time and space with the velocity of the tire

$$f = v f^{\text{s}}$$

results, for the example of $v = 80\,\text{km/h} = 22\,222.\bar{2}\,\text{mm/s}$, in the frequency bounds

$$f_{\min} = 0.678\,\text{Hz}$$
$$f_{\max} = 22.\bar{2}\,\text{kHz}.$$

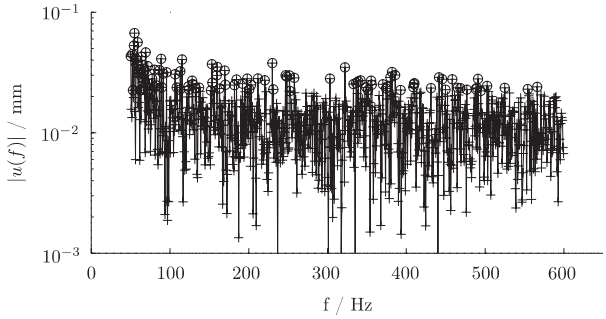

Fig. 11. Extraction (o) of excitation spectrum (-+-).

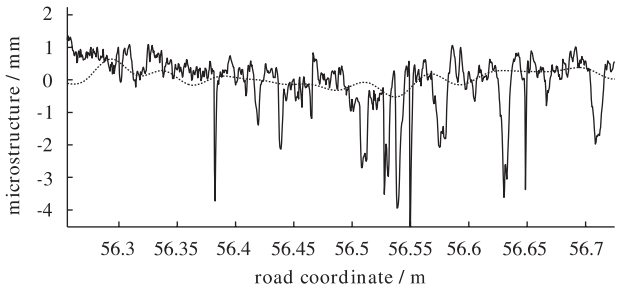

Fig. 12. Measurement (—) and Fourier synthesis (···).

Inversely one can say that for the frequency range of interest from 50 to 1500 Hz the spatial wavelength spectrum for the excitation of tires at velocities of 40−150 km/h is about 5 mm to 1 m. Texture components outside this range have no influence on the sound radiation at the important frequencies of this model. Besides this hard filtering in the frequency domain another filter is used to reduce the computational cost. The power spectral density is examined to extract the frequency components with the highest energy assuming they have the main virtue on the resulting vibrations. An example is shown in Fig. 11 for the 100 strongest amplitudes marked with circles in the frequency range 50−600 Hz. In Fig. 12 a section of the microstructure of the road and the reconstruction with the extracted components using Fourier synthesis is depicted. With this approach one is not attempting to avoid the computation of how deep the tire will go into the grooves of the real texture, since the frequency parts of the grooves have no importance.

4.5. Operational dynamics

Now the tire is subjected to the deterministic excitation of a split mastic asphalt and a concrete jute texture. The 400 smallest eigenpairs are used in conjunction with the complete spectrum of 1106 harmonic excitations between 100 and 850 Hz, depicted in Fig. 13. Since the rather coarse model investigated here may be analyzed within reasonable computing time without reduction of the spectrum, all components are taken into account.

The matrices of generalized coordinates, being the participation factors of an eigenform in the operational vibration associated with the excitation, are compared in Fig. 14, where the magnitudes of the complex matrix entries are plotted. Both subfigures have the largest entries on the diagonal axis, where resonance occurs, while more than 87% of the entries are smaller than 10^{-1}. This correlation shows that an excitation causes responses of the eigenvectors with similar eigenfrequency. Also this could be another starting-point for the reduction of computational cost. If a small matrix, that is moving over the diagonal entries, and the corresponding excitation functions as well as the eigenpairs are used to get the operation in this frequency range, the results can be superimposed afterwards for the full range with the advantage that the negligible entries in the whole matrix of generalized coordinates may not have to be considered. Comparing the two different textures, the magnitude of the peaks of split mastic asphalt is twice as large as of concrete jute texture. Besides this, the main peaks occur at different locations of the diagonal axis.

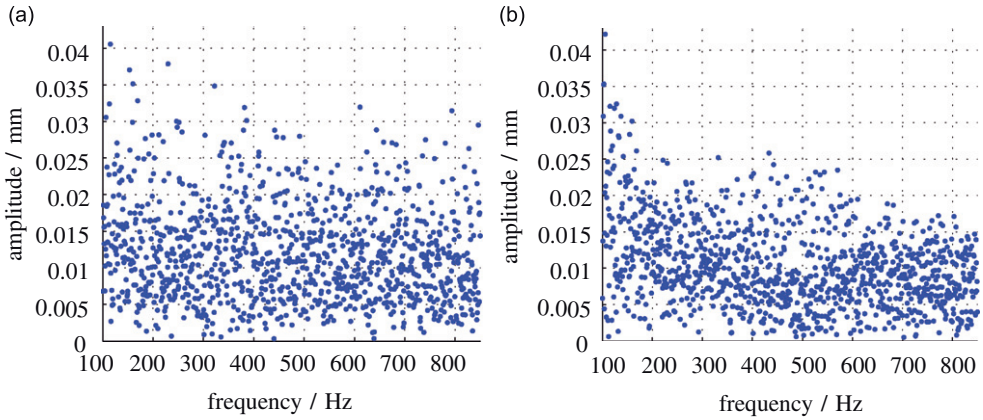

Fig. 13. Spectrum of the excitation of different textures: (a) split mastic asphalt; (b) concrete jute texture.

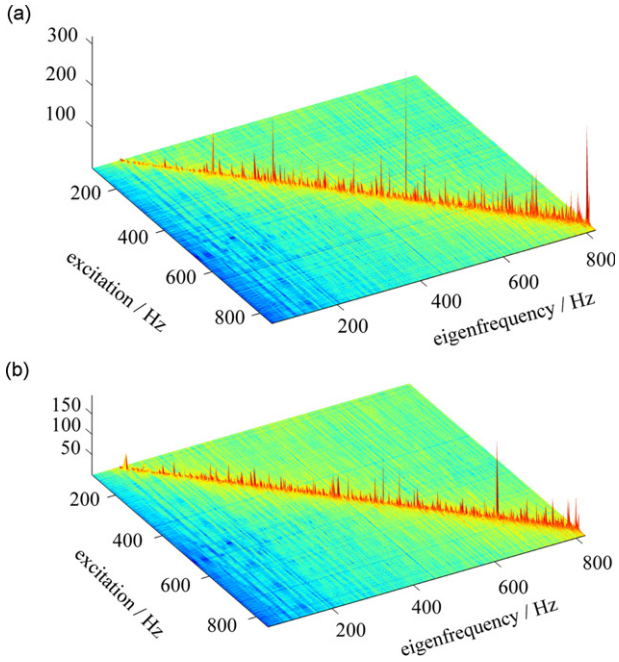

Fig. 14. Magnitude of entries in the matrices of generalized coordinates: (a) split mastic asphalt; (b) concrete jute texture.

Some snapshots at discrete timesteps of operational deflection shapes are shown in Fig. 15 for both textures. The effective nodal amplitude is color coded in the given decibel scale. Looking more closely at the footprint, one may identify the texture pattern moving to the left, while the tire is rolling to the right. The structural amplitude of the tire on the split mastic asphalt is larger then on the concrete jute texture, which will result in a higher sound pressure level. Another difference is the wavelength of the dominant eigenforms corresponding to the expansion of the zones of similar color, showing that the split mastic asphalt has short waves equal to high-frequency components. This is also recognizable in the spectrum of excitation in Fig. 13 showing the correlation between input and output of the model.

4.6. Acoustic analysis

The sound radiation is computed based on the structural dynamics of the rolling tire. For the simulations presented here, 400 eigenpairs up to a frequency of 822 Hz have been computed. The sound pressure has been

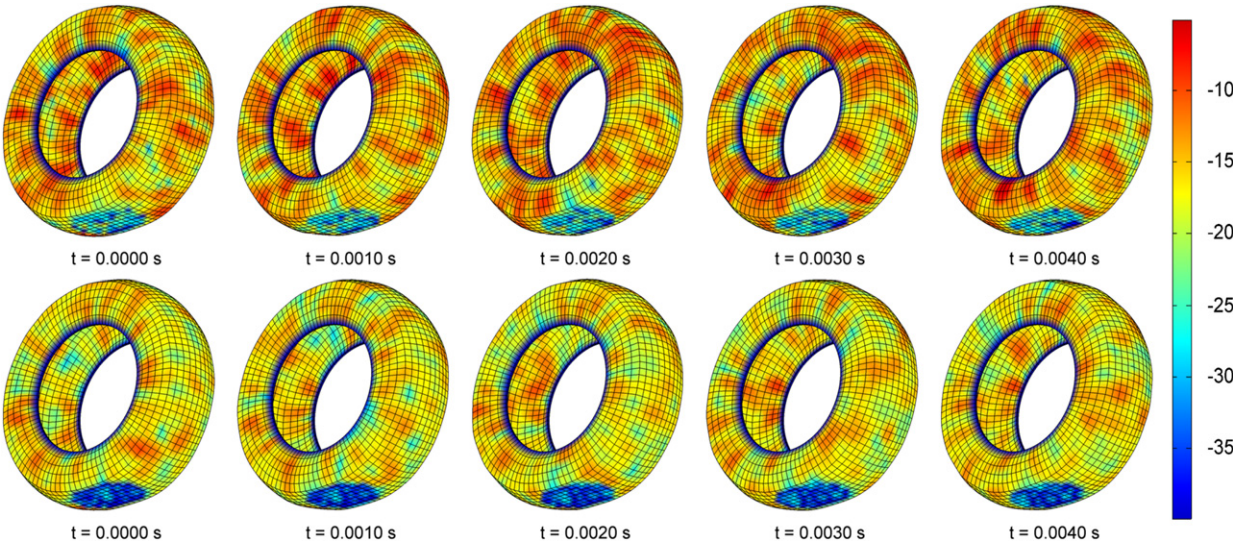

Fig. 15. Operational deflection shapes on split mastic asphalt (upper row) and concrete jute texture (lower row)—effective nodal amplitude in dB.

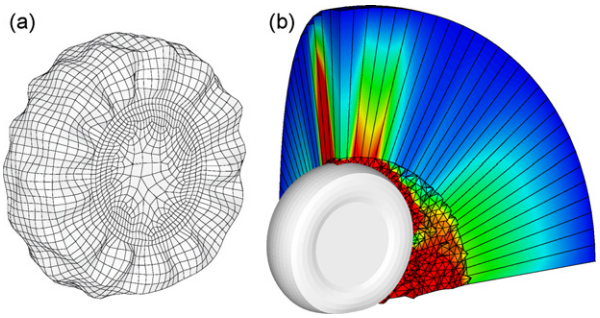

Fig. 16. Normal velocity at 642 Hz for concrete jute texture (a) and acoustic model with finite and infinite elements including the sound pressure amplitude (b).

computed for a total of 1106 excitation frequencies between 100 and 850 Hz, obtained from the roughness of the road surface (cf. Section 4.4). In this method the normal velocities on the tire surface were determined in each frequency step by superimposing the weighted eigenmodes. The resulting system was solved using the GMRES algorithm together with an incomplete LU factorization.

In order to analyze the influence of the mechanical excitation due to the roughness of the road, the acoustic characteristics of the road surface remain unconsidered here, i.e. the absorption has been assumed to be zero ($\alpha = 0$). Regarding the air, the usual fluid properties with density $\rho = 1.225\,\mathrm{kg/m^3}$ and wave speed $c = 340\,\mathrm{m/s}$ were adopted. The speed of the tire is 80 km/h.

Fig. 16(a) depicts the normal velocity of the tire at 642 Hz as a result of the excitation by the concrete jute texture. A section of the acoustic finite/infinite element model with a total of 17 458 degrees of freedom as well as the sound pressure distribution at 642 Hz are shown in Fig. 16(b).

Fig. 17 depicts the sound pressure amplitude for the excitation of the tire due to a concrete jute texture, evaluated at a field point located in the exterior part of the FE-model. According to the commonly used test set up when measuring the pass-by level, the field point is located at a height of 1.2 m and a distance of approximately 6.5 m to the tire center. For these simulations, however, the tire is spatially fixed. The dashed line in Fig. 17 represents the sound pressure amplitude in dB, while the solid line stands for the data in dB(A) using a third octave filter. The filtered data has a maximum of the acoustic pressure level in the spectrum around 400 Hz. The sound pressure amplitudes are very low in the lower frequency range due to the

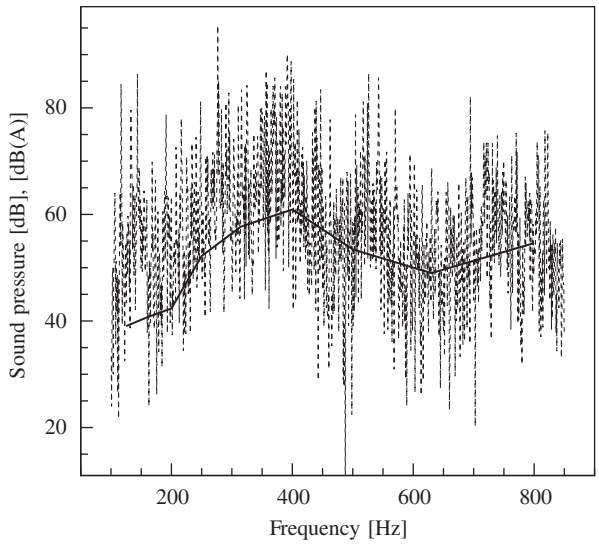

Fig. 17. Sound pressure amplitude for the concrete jute texture as raw data (- - -) in [dB] and as third octave band (—) in [dB(A)].

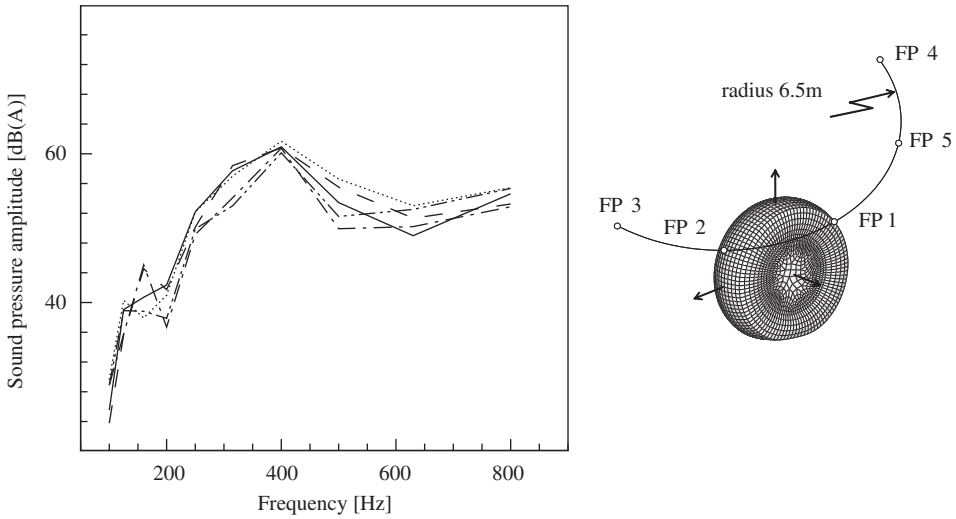

Fig. 18. Sound pressure level for different field point locations: FP 1 (—); FP 2 (- - -); FP 3 (-·-·-); FP 4 (···); FP 5 (-·-·-·-).

A-weighting. Note, that the results given in Fig. 17 may not be directly compared to experimental data from a pass-by test, since only the mechanical excitation due to the road roughness is considered.

The sound pressure evaluated at different field points is shown in Fig. 18. There, the field points are located on an arc, with a radius of 6.5 m, 1.2 m above the road surface, cf. Fig. 18, where the tire is rolling towards FP 3. For all field points, the results are given in Fig. 18. The maximum sound pressure level occurs in the frequency band around 400 Hz. The differences among the third-octave filtered sound pressure level for the different fieldpoint locations vary from roughly 7 to 1.5 dB(A) at 400 Hz. The largest weighted sound pressure level of 61.7 dB(A) occurs at FP 4.

A comparison of the two different road textures, namely a concrete jute texture and a split mastic asphalt, is shown in Fig. 19. In the lower frequency range, i.e. up to 315 Hz, only small differences occur. At 400 Hz, however, the difference in the sound pressure amplitude increases, where the sound pressure for the split mastic asphalt is about 2 dB(A) higher, i.e. representing the more noisy road surface (not considering acoustic impedance). The largest difference with approximately 3 dB(A) occurs at 500 Hz.

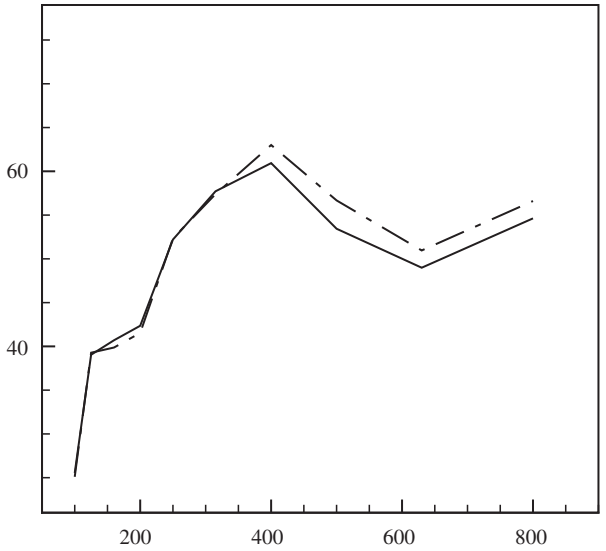

Fig. 19. Sound pressure level for two different road textures: concrete jute (—) and split mastic asphalt (-·-·-).

Table 1
Sound pressure level in the third octave band for the tire/road noise simulations

Frequency (Hz)	Sound pressure at field points (dB(A))			
	$SPL_{FP\,1}$	$\widetilde{SPL}_{FP\,1}$	$SPL_{FP\,3}$	$\widetilde{SPL}_{FP\,3}$
100	25.54	26.94	28.88	27.77
125	39.05	38.71	35.74	35.76
160	40.70	41.00	45.05	44.87
200	42.35	41.71	36.70	36.97
250	52.20	52.46	49.15	48.75
315	57.72	57.75	54.08	54.37
400	60.94	61.14	60.75	60.60
500	53.44	53.30	49.92	49.58
630	48.99	48.41	50.21	50.02
800	54.62	52.94	52.88	49.56

In Section 4.5 it has been discussed that large contributions to the right-hand side in Eq. (29) exclusively arise from eigenpairs in the vicinity of the excitation frequency (cf. Fig. 14). In order to save computational costs, only selected eigenpairs, close to the excitation frequency, may be considered when analyzing the dynamic response and the sound radiation. Sound pressure levels evaluated at two different field point locations are given in Table 1. In this simulation the sound pressure level was computed using contributions to the right-hand side from all 400 eigenvalues (denoted by SPL) and also neglecting eigenvectors outside a band of ± 50 Hz around the corresponding excitation frequency (denoted $\widetilde{SPL}$). While only small differences occur up to 630 Hz, it appears, that at higher frequencies around 800 Hz, the solution using only eigenmodes close to the excitation frequency deteriorates from the solution using the full set of eigenvectors. Hence, it seems necessary to enlarge the set of considered eigenpairs at higher frequencies.

5. Conclusions

A physically based computational model for the analysis of noise radiated from rolling tires has been presented in this contribution. The fundamentals of the underlying numerical methods for the study of tire

dynamics and the sound radiation have been described. The contribution focuses on the representation of the overall computational strategy and the employed numerical methods with respect to the simulation of tire/road noise. The overall model has been implemented adopting advanced state-of-the-art simulation techniques. This enables a detailed analysis of the tire/road system, rendering goal-oriented investigations of certain effects of the noise generation and radiation possible (e.g. constructional parameters of the tire, driving velocity, road roughness, impedance, etc.).

Simulations of the tire/road noise have been presented for frequencies up to 850 Hz and rather coarse discretizations of the tire/road system have been used. In order to simulate the tire/road noise within the relevant frequency range up to 1.5 Hz in a reliable way, the discretizations have to be refined. This further increases the demands regarding the efficiency of the methods used in the computational model.

Priority of future work is given to the appropriate validation of the current model. Therefore, measurements of different tire models rolling on a drum will be performed, monitoring the tire vibrations as well as the radiated sound. These will be compared to simulations with the same assembly as the real tires.

The present work demonstrate the computability of the suggested approach. The next step will focus on a sequential refinement of the finite element model based on the results from laboratory experiments. Additional effects, such as frequency dependent material behavior, slip–stick contact, and treat-pattern impact, will be addressed in a subsequent step.

Acknowledgements

The authors would like to thank the Federal Ministry of Education and Research (BMBF) in Germany for the financial support of this research work.

References

[1] U. Sandberg, J. Ejsmont, *Tyre/Road Noise Reference Book*, Informex, Kisa, Sweden, 2002.
[2] W. Kropp, K. Larsson, F. Wullens, P. Andersson, F. Becot, T. Beckenbauer, The modeling of tire/road noise—a quasi three-dimensional model, *Proceedings of the Internoise*, The Hague, Netherlands, 2001.
[3] de Roo F. TRIAS, tyre road interaction acoustic simulation model, *Proceedings of the Internoise*, The Hague, Netherlands, 2001.
[4] Y. Kim, J. Bolton, Effect of rotation on the vibration characteristics of tires, *Proceedings of the Internoise*, Dearborn, USA, 2002.
[5] U. Nackenhorst, The ALE-formulation of bodies in rolling contact—theoretical foundations and finite element approach, *Computer Methods in Applied Mechanics and Engineering* 193 (2004) 4299–4322.
[6] R. Lehoucq, D. Sorensen, C. Yang, Arpack users' guide: solution of large scale eigenvalue problems with implicitly restarted Arnoldi methods, SIAM Series in Software, Environments, and Tools 1998, 1997.
[7] F. Tisseur, K. Meerbergen, The quadratic eigenvalue problem (370). ⟨URL: http://citeseer.ist.psu.edu/tisseur01quadratic.html⟩.
[8] D. Dreyer, O. von Estorff, Improved conditioning of infinite elements for exterior acoustics, *International Journal for Numerical Methods in Engineering* 58 (6) (2003) 933–953.
[9] R.J. Astley, G.J. Macaulay, J.-P. Coyette, L. Cremers, Three-dimensional wave-envelope elements of variable order for acoustic radiation and scattering. Part I. Formulation in the frequency domain, *Journal of the Acoustical Society of America* 103 (1) (1998) 49–63.
[10] D. Dreyer, S. Petersen, O. von Estorff, Effectiveness and robustness of improved infinite elements for exterior acoustics, *Computer Methods in Applied Mechanics and Engineering* 195 (29–32) (2006) 3591–3607.
[11] B.S. Kirk, J.W. Peterson, libMesh (2004). ⟨http://libmesh.sourceforge.net⟩.
[12] R.J. Astley, Infinite element formulations for wave problems: a review of current formulations and an assessment of accuracy, *International Journal for Numerical Methods in Engineering* 49 (2000) 951–976.
[13] K. Gerdes, A review of infinite element methods, *Journal of Computational Acoustics* 8 (1) (2000) 43–62.
[14] J.J. Shirron, S. Dey, Acoustic infinite elements for non-separable geometries, *Computer Methods in Applied Mechanics and Engineering* 191 (2002) 4123–4139.
[15] J.-P. Coyette, B. Van den Nieuwenhof, A conjugated infinite element method for half-space acoustic problems, *Journal of the Acoustical Society of America* 108 (4) (2000) 1464–1473.
[16] D. Dreyer, Efficient Infinite Elements for Exterior Acoustics, PhD Thesis, TUHH, Shaker Verlag, 2004.
[17] J. Cipolla, Acoustic infinite elements with improved robustness, in: P. Sas, B. Van Hal (Eds.), *Proceedings of ISMA 2002*, Katholieke Universiteit Leuven, 2002, pp. 2181–2187.
[18] F. Ihlenburg, On fundamental aspects of exterior approximations with infinite elements, *Journal of Computational Acoustics* 8 (1) (2000) 63–80.

[19] J.M.M.C. Marques, D.R.J. Owen, Infinite elements in quasi-static materially nonlinear problems, *Computers and Structures* 18 (4) (1984) 739–751.
[20] W. Eversman, Mapped infinite wave envelope elements acoustic radiation in a uniformly moving media, *Journal of Sound and Vibration* 224 (4) (1999) 665–687.
[21] J.A. Hamilton, R.J. Astley, Acoustic propagation on irrotational mean flows using transient finite and infinite elements, *AIAA Journal* 43 (1) (2005) 124–134.
[22] U. Nackenhorst, Rollkontaktdynamik, Numerische Analyse der Dynamik rollender Körper mit der Finite Elemente Methode, Habilitation Thesis, 2000.